

OPEN ACCESS

State-of-Health Diagnosis of Lithium-Ion Batteries Using Nonlinear Frequency Response Analysis

To cite this article: Nina Harting *et al* 2019 *J. Electrochem. Soc.* **166** A277

View the [article online](#) for updates and enhancements.



Connect with decision-makers at ECS

Accelerate sales with ECS exhibits, sponsorships, and advertising!

▶ Learn more and engage at the 244th ECS Meeting!



State-of-Health Diagnosis of Lithium-Ion Batteries Using Nonlinear Frequency Response Analysis

Nina Harting,^{1,2} Nicolas Wolff,^{1,2} Fridolin Röder,^{1,2} and Ulrike Krewer^{1,2,z}

¹Institute of Energy and Process Systems Engineering, TU Braunschweig, Braunschweig, Germany

²Battery LabFactory Braunschweig, TU Braunschweig, Braunschweig, Germany

Estimation of the State-of-Health (SOH) of Lithium-ion Batteries (LIBs) is commonly conducted using in-situ measurement methods, such as Incremental Capacity Analysis (ICA) and Differential Voltage Analysis (DVA) as well as impedance based techniques. In this study, we present an alternative method for SOH estimation: The nonlinear dynamic measurement method Nonlinear Frequency Response Analysis (NFRA) is shown to be able to estimate capacity fade of LIBs due to loss of active material. Capacity loss correlates with the quotient of the root mean square of the second and the third harmonic response for different excitation amplitudes in the frequency range sensitive to electrochemical reactions at approximately 1 Hz. The results of the experimental cycle-aging study are validated and further analyzed by using a reaction model containing Butler-Volmer kinetics with a dynamic charge balance of the electrode. Simulations show that the NFR quotient and capacity fade due to loss of specific surface area correlate exactly. We identify the NFR quotient as a reliable, easily measurable parameter for the diagnosis of the SOH of LIBs. Therefore, this study reveals a novel approach for SOH estimation of LIBs based on dynamic analysis with NFRA.

© The Author(s) 2019. Published by ECS. This is an open access article distributed under the terms of the Creative Commons Attribution Non-Commercial No Derivatives 4.0 License (CC BY-NC-ND, <http://creativecommons.org/licenses/by-nc-nd/4.0/>), which permits non-commercial reuse, distribution, and reproduction in any medium, provided the original work is not changed in any way and is properly cited. For permission for commercial reuse, please email: oa@electrochem.org. [DOI: 10.1149/2.1031902jes]



Manuscript submitted August 16, 2018; revised manuscript received November 26, 2018. Published January 28, 2019.

Reliable and precise state diagnosis of Lithium-ion Batteries (LIBs) is essential for estimating cycle life and reducing safety risks of battery systems used in electric vehicles (EVs).¹ This includes an exact and accurate estimation as well as monitoring of the State-of-Health (SOH) of the battery cells. Manifold aging processes lead to a distinct decrease of the usable capacity and to an increase of the internal resistance of the LIB.²⁻⁴ Additionally, aging processes are complex and always depend on the cell chemistry and design. Three main categories of LIB aging mechanism are often distinguished, i.e. loss of active material, loss of lithium inventory and reduced conductivity.⁵ In general, degradation of LIBs includes performance loss of the battery and therefore leads to a loss of driving range per charge of EVs.⁴ Thus, the accurate diagnosis of SOH is an indispensable part of effective battery health management of every battery management system (BMS).⁶

Typically, BMS use capacity decrease and power fade with regard to the nominal values to quantify the SOH.⁷ Other approaches use the internal resistance R_0 for the estimation of the SOH.⁸⁻¹¹ For the measurement of cell capacity, in-situ techniques are proposed, e.g. Incremental Capacity (IC),¹² Differential Voltage (DV),¹³ combined IC-DV techniques⁵ as well as Electrochemical Impedance Spectroscopy (EIS).¹⁴ IC-DV and EIS are thereby suitable for SOH diagnosis as well as identification and differentiation of various aging mechanisms.^{5,15} Both methods have specific advantages in regard to SOH estimation. EIS has shorter a measurement time and can be used at particular frequencies and State-of-Charges. In contrast, IC-DV comes with a long test duration of approximately 10 hours per cell.¹⁴ However, IC-DV is superior to EIS in regard to the universal, model-independent application and low-cost hardware implementation as well as easy calculation.⁵ Nevertheless, the LIB has to be in a steady-state for both diagnosis techniques. In general, an efficient BMS benefits from a fast, cheap and accurate on-board SOH diagnosis of state and cycle life of LIBs.^{6,16}

EIS is the most commonly applied method for state and process characterization of LIBs.^{15,17} With EIS, a small sinusoidal current I_{AC} for linear system excitation is applied. According to literature, electrochemical and physical processes in the cell cause distinct, characteristic signals in the resulting impedance spectra. LIBs, however, are systems with a nonlinear relation between current and voltage, e.g. as for Butler-Volmer kinetics. Capacitive effects, such as charging and

discharging of double-layers can show a nonlinear relation of current and voltage.¹⁸ Further, diffusion in the spherical particles is coupled to the electrochemical reactions via the activity of Lithium at particle surface, which is a nonlinear function of concentration. Those processes cause specific nonlinearities measurable by Nonlinear Frequency Response Analysis (NFRA), which we demonstrated in our previous studies.^{19,20} Nonlinear analysis methods have been already used in the field of electrochemical analysis and concentration sensing of fuel cells^{21,22} and for the SOC estimation on lead acid batteries.²³

Further, NFRA has been shown in the last two years to be applicable to characterize operating processes and aging of LIBs.^{19,24,25} Different measurement and interpretation approaches have been used to study the nonlinear voltages responses of LIBs. The main reason why there is some diversity in measurements and interpretation for nonlinear analysis is that in contrast to EIS, nonlinear system analysis has no standardized unique theory based on control engineering, and it is not yet clear how to best trigger, analyze and interpret nonlinear responses. Our research is focused on the analysis of individual harmonic voltage responses as well as the root mean square of the second and third harmonic excited by sinusoidal currents with amplitudes of $>1C$ in the overall frequency range. Another approach is used by Murbach et al., who apply moderate nonlinear currents between 0.2–0.3C at frequencies higher than 10 Hz to analyze experimentally the second harmonic voltages as well as the phase shift in the Nyquist domain.²⁵ Additionally, it has been demonstrated that modeling NFRA is the key for an in-depth understanding and thus better interpretation of NFR spectra, e.g. to understand the effect of particle size on spectra or the origin of a given high nonlinearity at a certain frequency.^{20,24} Simulations drastically enhanced and verified process identification of LIBs using NFRA.^{20,24} Further, Harting et al. discovered that it is possible to identify the crucial aging effect Lithium plating based on their nonlinear dynamics, as plated cells cause specific nonlinear voltage responses.²⁶ By only analyzing the linear system behavior with a linear amplitude I_{AC} , sensitive and valuable dynamic information about nonlinearity is lost. Recently, we presented an effective data-driven identification of the SOH of LIBs based on a degradation model using Support Vector Regression derived from NFRA.²⁷

In this paper, we propose NFRA as a possible alternative method to established diagnosis methods for SOH estimation. We present NFRA in a novel quantification approach for the SOH estimation by correlating specific NFR-based signals to cyclic-aging induced capacity fade of LIBs. Therefore, we explicitly take advantage of the characteristic, highly informative dependency of nonlinear cell processes on the

^zE-mail: u.krewer@tu-braunschweig.de

excitation amplitude I_{AC} , which has not been analyzed yet. In detail, the ratio of nonlinearities of two different AC excitation amplitudes I_{AC} is shown to correlate to capacity fade of LIBs in characteristic frequency ranges. Additionally to experiments, a surface reaction model based on Butler-Volmer kinetics, is applied to give a physical reasoning for the proposed measurement method, as our focus in this study is to give an extensive insight into how and why the method is feasible for SOH diagnosis. As such, a detailed comparison with other SOH diagnosis methods is out of scope of this work and should be done in future with a focus on robustness and limitations of each method.

Theory

Nonlinear frequency response analysis.—With NFRA, a sinusoidal input signal with high current amplitude I_{AC} is applied to the system in a defined frequency range from mHz to kHz. Changes in the sinusoidal output voltage U_{AC} in time domain are measured. By applying a Fast-Fourier Transformation (FFT), the sinusoidal voltage output signal U_{AC} is transferred from the time to the frequency domain. However, not only the voltage signal corresponding to input frequency Y_1 as in EIS, but also higher harmonic responses Y_n with $n > 1$ can be detected. Higher harmonic amplitudes of the responses, Y_2 to Y_n , are observed at multiples of the fundamental frequency f_1 of the sinusoidal input signal:

$$f_n = n \cdot f_1 \quad [1]$$

Due to their different parities, even Y_{2n} as well as odd harmonics Y_{2n+1} each have a different characteristic dependency on the input amplitude and frequency. Their intensity decreases with increasing n . We have examined this dependency for Lithium-Ion batteries in our previous work, by investigating individual higher harmonic responses Y_n as well as the square root of the squares of all higher harmonics over the inset frequency.¹⁹

In this and future studies we recommend to use the root mean square of the first two harmonics given in Equation 2 instead of the sum of all higher harmonics, or the square root of the squares of the higher harmonics, which we used in past work,^{19,26,27} because the rms is a well known measure in metrology and electrical engineering, also for THD,²⁸ and it gives a sound mean value of overall nonlinearity of a system.

$$Y_{rms} = \sqrt{\frac{\sum_{n=2}^3 Y_n^2}{2}} \quad [2]$$

As the rms requires division by the number of higher harmonics, comparability of rms will be only given if the same number of higher harmonics is used. Distinct nonlinearities are visible for Y_2 and Y_3 , and their comparison allows to distinguish between aging phenomena.²⁶ The amplitudes are therefore chosen so that nonlinear responses for Y_2 and Y_3 are visible, but all further higher harmonics, i.e. $i > 3$, are negligible. This also prevents interference of the signals.²⁹

In our study, we introduce a dynamic analysis parameter for aging quantification of LIBs based on NFRA. The NFRA quotient λ is defined as the ratio of the root mean square of the second and the third harmonic response measured with a higher sinusoidal amplitude I_{AC1} and the root mean square of the second and the third harmonic response measured with a different, smaller amplitude I_{AC2} .

$$\lambda = \frac{\sqrt{\frac{\sum_{n=2}^3 Y_n^2}{2}} I_{AC1}}{\sqrt{\frac{\sum_{n=2}^3 Y_n^2}{2}} I_{AC2}} \quad [3]$$

The correlation of this frequency dependent value to SOH is analyzed.

Reaction model.—For an in-depth analysis of the presented capacity estimation, a reaction model is used. The focus of the model is to

Table I. Simulation parameters used in the reaction model.

Parameter	Symbol	Value	Unit
Initial potential	$E(0)$	0	V
Exchange current density	i_0	10	A m^{-2}
Double layer capacitance	C_{DL}	18	F m^{-2}
Temperature	T	300	K
Particle radius	R_p	$10 \cdot 10^{-6}$	m
Volume fraction of active material	$\varepsilon_{s,0}$	0.6	-
Symmetry factor	α	0.5	-

investigate the degradation of LIBs due to loss of specific surface area of the electrode at a given SOC and therefore one single electrochemical reaction is implemented and lithium accumulation is neglected in all phases. Transport processes in the electrode and electrolyte as well as the process dependency of the open circuit voltage are neglected in the model. The base case parameter set is provided in Table I and parameters are chosen to be in broad range suitable for LIBs.³¹ All functions are embedded in Matlab, and time derivatives are solved with an ode-15s-solver. The reaction model contains a charge transfer reaction following Butler-Volmer kinetics:

$$j_{Li} = a_s j_0 \left(\exp\left(\alpha \frac{z\eta F}{RT}\right) - \exp\left(- (1-\alpha) \frac{z\eta F}{RT}\right) \right), \quad [4]$$

where j_{Li} is the current density generated for the reaction of Lithium, a_s is the specific surface area of the electrode, j_0 is the exchange current density, F is the Faraday constant, R is the ideal gas constant, T the temperature and η the overpotential, which is calculated as following:

$$\eta = \Delta\phi - E(0), \quad [5]$$

with the electrical potential difference $\Delta\phi$ and the initial potential $E(0)$, which is set to a constant value. Further, charge and discharge of the electrochemical double layer at electrode/electrolyte interfaces is implemented as:

$$a_s \cdot C_{DL} \frac{\partial \Delta\phi}{\partial t} = j_{DL}, \quad [6]$$

where C_{DL} is the electric double layer capacitance, $\Delta\phi$ is the electrical potential difference, and j_{DL} is the volumetric current density of the electrochemical double layer. Both volumetric rates, j_{Li} and j_{DL} sum up to the total current leaving/entering the electrode.

$$j_{tot} = j_{Li} + j_{DL}. \quad [7]$$

The specific surface area of the electrode a_s , is calculated as

$$a_s = 3 \frac{\varepsilon_s}{R_p} \quad [8]$$

using the particle radius R_p and the volume fraction of active material ε_s .³¹

The capacity loss as an aging effect of LIBs is simulated based on the approach that active material loses the contact to the matrix of conducting additives and binder, for example by particle cracking.³⁰ Thus, the decreasing amount of active material, respectively capacity, is implemented via decreasing the volume fraction of active material ε_s . Due the implementation of one single electrochemical reaction, ε_s is not specific to anode or cathode and therefore the initial volume fraction of active material $\varepsilon_{s,0}$ is a chosen value. $\varepsilon_{s,i}$ is calculated following the experimentally determined capacity loss, given in Equation 9. This correlation is defined as:

$$C = C_0 \frac{\varepsilon_{s,i}}{\varepsilon_{s,0}} \quad [9]$$

where $\varepsilon_{s,0}$ is the initial volume fraction of active material, $\varepsilon_{s,i}$ the volume fraction of active material after i cycles and C_0 the initial capacity. This leads to a smaller specific surface area of the electrode a_s , according to Equation 8. Thereby, as shown in Equation 4, the current density j_0 has to increase, if the same current I_{AC} is applied

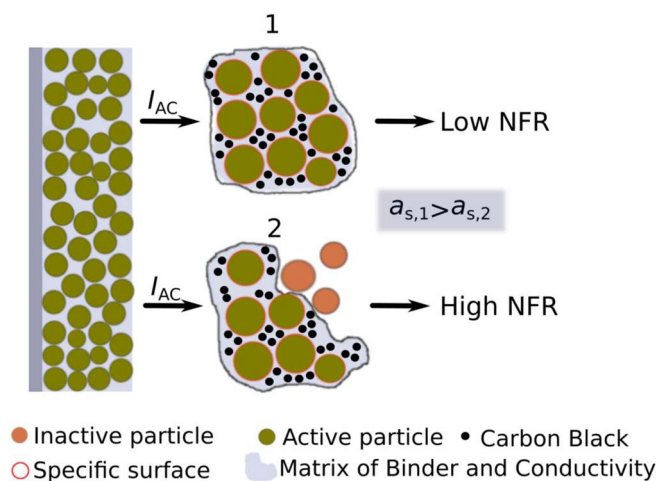


Figure 1. Schematic illustration of (1) an electrode with original matrix of binder and conductivity and (2) an aged electrode after cyclic aging due to loss specific surface area a_s , e.g. due to loss of active material in the matrix of binder and conductivity.

to the reaction model. In Figure 1, aging process of the electrode is illustrated schematically. To analyze cell dynamics, NFR spectra are simulated using the reaction model. For this purpose, an excitation current I_{AC} is applied to the model and the voltage output U_{AC} in the time domain is transferred to the frequency domain using a Fast-Fourier Transformation (FFT). As in the experiments, the root mean square of the second and third harmonic is calculated (Equation 2).

Experimental

Cell specifications.—Single layer Lithium-ion pouch cells with NMC as cathode, graphite as anode and a Celgard 2320 separator were used in this study. Electrodes were obtained from Battery Lab-Factory Braunschweig (BLB). As electrolyte, a solvent mixture of ethylene carbonate, dimethyl carbonate and ethyl methyl carbonate (EC/DMC/EMC) with a ratio of 1:1:1 with 2% Vinyl chloride (VC) and 3% cyclohexylbenzene (CHB) as additives and 1 M LiPF₆ as conducting salt were used. The inactive components are polyvinylidene fluoride (PVDF) as binder and carbon black (CB) as conducting additives. The characteristic cell parameters are listed in Table II and initial capacity C_0 and resistance R_0 as representative performance parameters in Table III. The specific surface area of anode $a_{s,a}$ and cathode $a_{s,c}$ can be calculated from the given parameters with Equation 8.

Measurements.—NFRA and EIS were measured with a Zahner Electrochemical Workstation (Zennium E) in galvanostatic mode. The frequency range was set between 20 mHz and 5 MHz, discretized with ten frequencies per decade above 66 Hz and five frequencies per

Table II. Cell parameters.

Parameter	Symbol	Unit	Anode	Separator	Cathode
Thickness ^a	δ	μm	55.25	20	60
Calendering degree	Π	%	40	-	25
Mass fraction of active material ^a	ζ	wt%	0.91	-	0.90
Mass fraction of inactive compounds ^a	ζ_{add}	wt%	0.09	-	0.10
Porosity ^b	ε	-	0.35	0.50	0.40
Geometric surface area ^b	A_{geo}	cm^2	35	-	29.25

^ameasured.

^bcalculated from manufacturer data.

Table III. Initial performance parameters.

Parameter	Symbol	Unit	Value
Initial capacity ^a	C_0	mAh	47
Initial resistance ^a	R_0	Ω	0.23

^ameasured.

decade for frequencies below 66 Hz. Amplitudes of higher harmonic responses from the 2nd (Y_2) to the 10th harmonic (Y_{10}) are measured and measurement noise is recorded. Measurements were performed in a temperature chamber at a constant environmental temperature of 25°C, if not further declared. If frequencies greater than 0.1 Hz are measured, changes of the open circuit voltage (OCV) are negligible, as OCV changes are approximately 1% under the measurement conditions used in the presented study. Thereby, changes in the NFR spectra can be assigned to changes of the investigated LIBs being at equilibrium. Applying sinusoidal currents with a high amplitude may damage the cell and enhance aging. However, whether and in what extent cell aging may be caused by NFRA strongly depends on the measurement conditions. For example, lithium plating may be caused, if a low-frequency AC current with a high amplitude is applied to cell at very high SOCs at low temperatures.³ In the presented study, measurement conditions of dynamic analysis are set to SOC 50% and 25°C, and thereby should prevent aging caused by high SOC operation. As well, an AC excitation may enhance aging, if it is constantly superimposed on a direct current load during long time cycling studies due to additional heat generation.^{34,35} For our studies, the impact of internal cell heating on NFR spectra was shown to be negligible for the measured LIBs.¹⁹ Thus the cell is assumed to be isothermal and additional aging due to the excitation signal is considered negligible.

Aging of LIBs was conducted by cycling with 1 C constant current (CC)/constant voltage (CV) charging until $I_{CV} \leq C/20$ and 1 C CC discharging in a potential window between 2.9 V and 4.2 V at 25°C using a MACCOR Battery Test System (Model 4200). Dynamic measurements were performed prior to aging and after each 50th cycle. The amplitude for EIS was set to 2 mA ($C/20$). NFRA was measured with three amplitudes I_{AC} of 20 mA (0.5 C), 50 mA (1.1 C) and 100 mA (2.3 C). Details for the dynamic measurements are listed in Table IV.

Results and Discussion

Process identification.—Prior to analyzing and discussing SOH diagnosis, typical frequency ranges for processes have been identified in the NFR spectrum of the unaged LIB in Figure 2, according to our previous publications.^{19,20} Processes in the low- to mid-frequency range Ia and Ib from 0.02 Hz to 10 Hz may be attributed to diffusion processes in active material particles and electrochemical reactions. Processes in frequency range II, which show significantly lower harmonic responses than the processes in range I, may be attributed to ionic transport processes such as migration, between and in the SEI and electrolyte. Those processes, typically, show almost constant,

Table IV. Measurement parameters of the dynamic analysis performed in defined cycling steps.

Parameter	Symbol	NFRA	EIS
Input Amplitude	I_{AC}	0.5 C/1.1 C/2.3 C	0.05 C
Frequency	ω	0.02 Hz to 10 ⁴ Hz	0.02 Hz to 10 ⁶ Hz
Measurement points	n_p for $\omega < 66\text{Hz}$	5	10
Measurement points	n_p for $\omega > 66\text{Hz}$	5	10
State of Charge	SOC	50%	50%

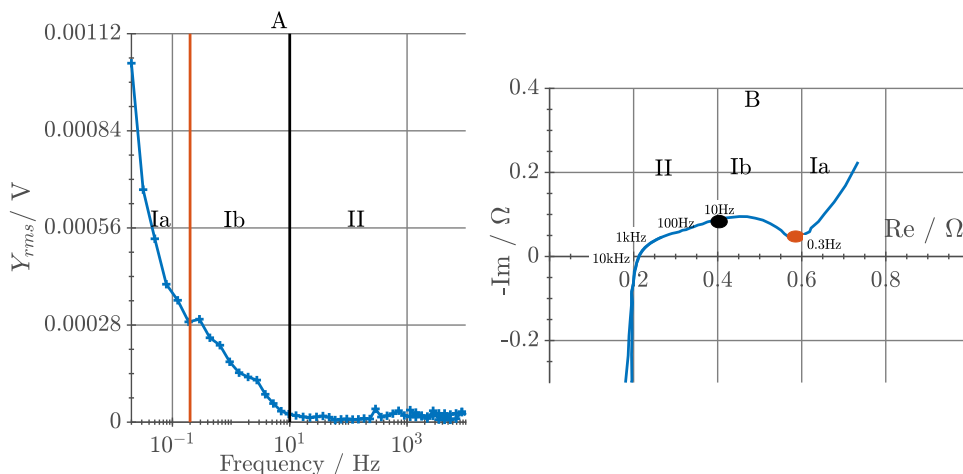


Figure 2. (A) NFR spectrum and (B) impedance spectrum measured with $I_{AC,EIS}=0.1$ C and $I_{AC,NFRA}=2.3$ C prior to cycle-aging.

minor higher harmonic responses than higher harmonic responses of electrochemical reactions of the electrodes in range Ia and Ib.¹⁹ However, the separation of range Ia and Ib at approximately 0.3 Hz is not as distinct for the cells tested in this study as for the cells of our previous study.¹⁹ This demonstrates that NFRA highly depends on the cell specifications and cell type.²⁰

The correlation of processes to frequency ranges is supported by process characterization in the impedance spectrum in Figure 2B. Roughly, two overlaying semi-circles can be identified. One semi-circle with a characteristic frequency at approximately 1 kHz and a second semi-circle with a characteristic frequency at approximately 10 Hz. However, these semi-circles are not clearly distinguishable. According to literature, the higher frequency semi-circle corresponds to the ionic transport reactions at the interface of electrolyte and SEI and the lower frequency semi-circle corresponds to the electrochemical reactions.^{32,33} A further indicator supporting this correlation is that the cell shows distinct and characteristic NFR in frequency range Ib, which corresponds perfectly to the lower-frequency semi-circle, which ranges from 0.3 to 10 Hz and is marked between the black and orange bullet in the impedance spectrum. Region Ib is separated from lower frequency responses by a characteristic small minimum and from the high frequency part, where nonlinearity is negligible. These three characteristic regions and their frequency ranges correspond perfectly to the three regions visible in EIS. The lower frequency

range for frequencies <0.3 Hz in the impedance as well as in the NFR spectrum corresponds to the diffusion process, which is in strong agreement to identification and correlation carried out in our previous publications.^{19,20,26}

Experimental aging analysis.—In Figure 3A, NFR spectra at three amplitudes $I_{AC}=0.5$ C, 1.1 C and 2.3 C, prior to aging are shown. Y_{rms} increases with increasing amplitude I_{AC} in frequency range Ia and Ib. In range II, Y_{rms} is almost independent of I_{AC} amplitude. This confirms that in frequency range II only processes with a minor nonlinear current-voltage relation and most probably no processes with a Butler-Volmer kinetic are excited. In the following aging study, NFRA measured with an excitation amplitude of I_{AC} of 0.5 C is not further considered for the analysis due to small nonlinear values. In Figures 3B and 3C, NFR signals for cycle aged LIB measured with $I_{AC2}=1.1$ C and $I_{AC1}=2.3$ C are shown after 0, 75, 215, 320 and 350 cycles. In general, Y_{rms} increases with number of cycles. Further, Y_{rms} is higher for a higher excitation amplitude I_{AC} . Y_{rms} excited with $I_{AC1}=2.3$ C are approximately one order of magnitude higher than Y_{rms} excited with $I_{AC2}=1.1$ C.

In a first step of mapping NFRA and capacity loss, Y_{rms} is extracted at the characteristic frequencies listed in Table V. In Figure 4, we choose to show the inverse of Y_{rms} over cycles instead of Y_{rms} , because the inverse decreases during aging. Thereby, a better quantitative

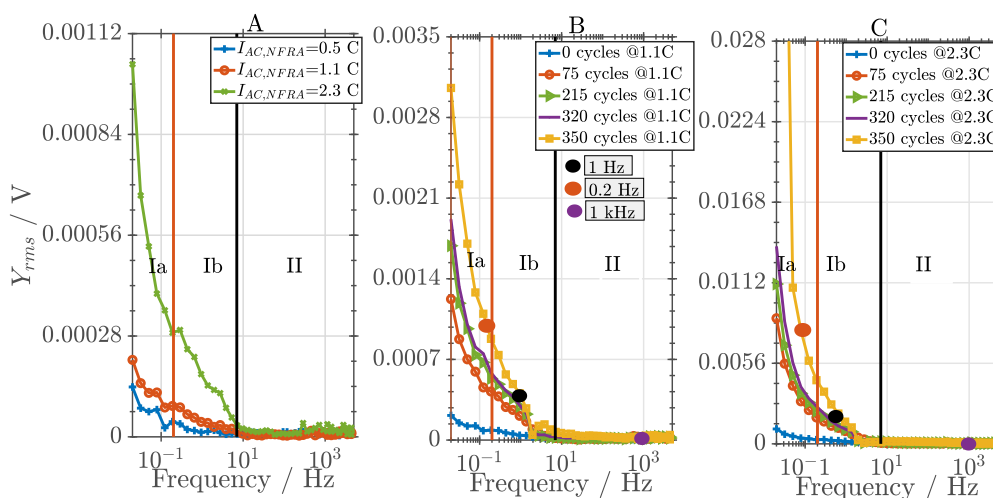


Figure 3. (A) NFR spectra measured with three amplitudes $I_{AC}=0.5$ C, (1).1 C and 2.3 C prior to cycle-aging, (B) during cycle-aging for $I_{AC,NFRA}=1.1$ C and (C) for 2.3 C.

Table V. Characteristic time constants and frequencies identified from NFR measurements.

Range	Time constant τ/s	Characteristic frequency range ω -range/Hz	Characteristic frequency $\omega_{process}/Hz$	Process
Ia	50 to 3	0.02 to 0.3	0.2	Solid diffusion
Ib	3 to 0.1	0.3 to 10	1	Electrochemical reactions
II	0.1 to 0.0001	10 to 10000	1000	Ionic transport processes at interfaces

correlation to the progression of the capacity decrease is possible. In Figures 4A to 4F, cell capacity loss and the inverse of Y_{rms} at the three characteristic frequencies $\omega_{process}$ is shown with cycling. Starting with an initial capacity C_0 of 47 mAh, which corresponds to a SOH of 100% at 0 cycles, the capacity decreases to 34 mAh, which corresponds to a SOH of 72.3%, at 75 cycles. Afterwards, it increases again slightly to 37 mAh after 275 cycles and to 38 mAh after 295 cycles. At the end of cycle-aging at 350 cycles, the capacity of the cell is 37 mAh, which corresponds to a SOH of 78.8%. As the capacity of the cell decreases during aging whereas Y_{rms} increases, we choose to show the inverse of Y_{rms} over cycles, which decreases during aging, for a better quantitative correlation of the progressions. At 1 kHz, the progression of the inverse of NFR strongly differs from the progression of the capacity fade for both excitation amplitudes, shown in Figures 4C and 4F. As partly Y_{rms} increases with SOH and partly decreases, and trends for the two amplitudes differ strongly, Y_{rms} and SOH cannot be correlated at 1 kHz. Thus, this is in correlation to the process identification in our previous studies, in which NFR excited in range II, characteristic for ionic transport processes between the SEI and electrolyte, has been identified to be not sensitive to aging mechanism of LIBs.^{19,26}

At 0.2 Hz, shown in Figures 4A and 4D, as well as at 1 Hz, shown in Figures 4B and 4E, however, a correlation between the inverse of NFR and the capacity can be identified for both excitation amplitudes. As expected, the inverse of Y_{rms} decreases for decreasing capacity for most cycles. However, there are deviations from this characteristic behavior, e.g. at 45 and 290 cycles. At 45 cycles, the inverse of Y_{rms} increases slightly for a lower capacity compared to previous cycles for both excitation amplitudes. However, this increase is only small and corresponds to a Y_{rms} decrease in the μV range, which is in the range of measurement uncertainty due to an accuracy of the device of $\pm 250 \cdot 10^{-6}$ V. At 290 cycles, however, the inverse of Y_{rms} decreases sharply for both excitation amplitudes at 1 Hz and for the higher excitation amplitude at 0.2 Hz, as well. In contrast to this, the inverse of Y_{rms} increases strongly at this cycle for the lower excitation amplitude at 0.2 Hz. These intense spikes of Y_{rms} are out

of the range of measurement uncertainties and indicate either specific, yet not understood changes in the cell or external disturbances of unknown source occurring right after the 290th cycle. Therefore, the correlation of the inverse of Y_{rms} to the capacity decrease is not considered to be reliable at these cycles. Further, it is noticed that the inverse of Y_{rms} decreases even if the capacity measured stays constant over multiples cycles, e.g. from 35 to 75 cycles, for both excitation amplitudes at 0.2 Hz and 1 Hz. Thereby, it is shown that it may not be possible to perfectly match the residual capacity to the overall Y_{rms} values. However, a general correlation between Y_{rms} and cycling can be identified. We assume that Y_{rms} not only correlates to aging processes decreasing the cell capacity respectively the specific surface area a_s , e.g. loss of active material of the matrix of binder and conductivity, but also to aging processes, such as conductivity loss, which increases the overall internal cell resistances.² Loss of specific surface area a_s includes a reduction of the maximal extent of lithiation of the electrodes and therefore the decreasing cell capacity. Y_{rms} may increase due to both aging types, capacity and power fade.

In a next step, the capacity decrease is correlated to λ for aging quantification of LIBs based on NFRA, as introduced in previous sections. The quotient λ is deduced from the performance efficiency, Θ , of LIBs, which can be used to quantify and monitor the performance of LIBs at different discharging currents from typically used cycle rate tests.^{36,37} For calculating Θ , the capacity at a higher discharging current is correlated to the capacity at a lower discharging current. Ideally, the capacity of the LIB at the higher current is close to the capacity at the lower discharging current. A performance efficiency Θ close to 1 is an indicator for a high performing LIB in contrast to a LIB with a lower Θ . In the following, this approach is transferred on NFRA for quantifying aging and estimating the SOH. Therefore, it is expected that the ratio λ decreases over cycling, as nonlinearities of the LIB increase for decreasing cell capacity at the corresponding excitation amplitudes, as demonstrated in the previous section.

In Figures 5A to 5C, the ratio λ of the root mean square of the second and the third harmonic response measured at $I_{AC1}=2.3$ C and

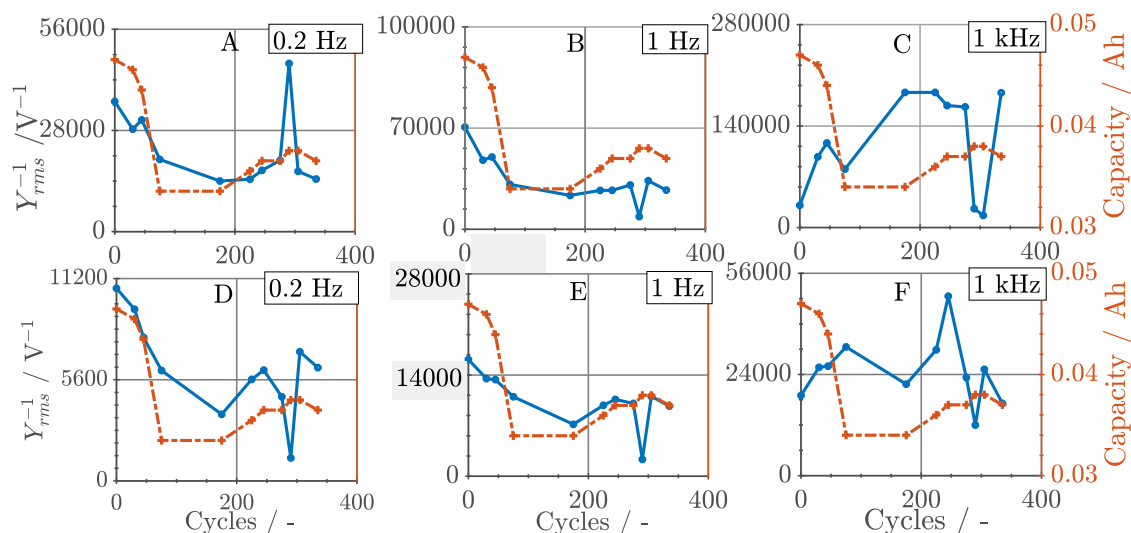


Figure 4. The inversed absolute values of Y_{rms} measured with $I_{AC2}=1.1$ C (top) and $I_{AC1}=2.3$ C (bottom) and cell capacity shown for cycle-aging at three characteristic frequencies: (A and D) 0.2 Hz, (B and E) 1 Hz and (C and F) 1 kHz.

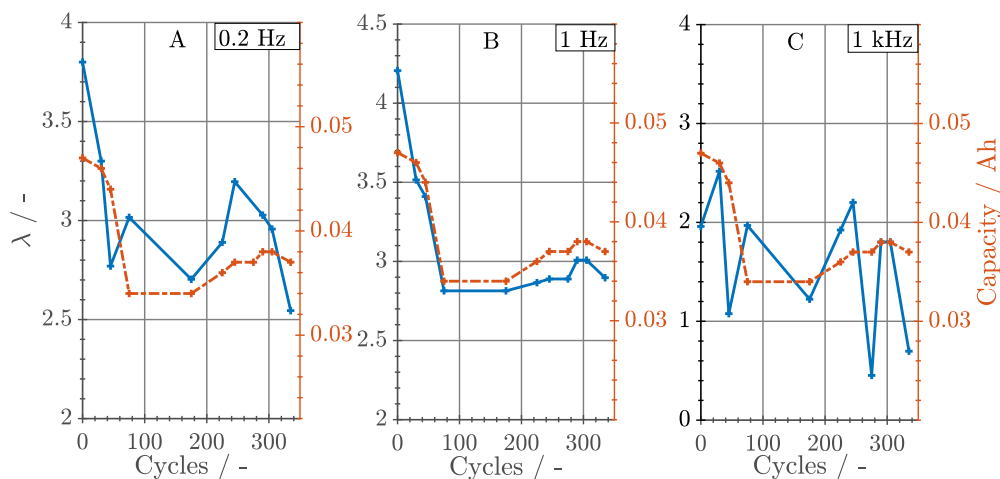


Figure 5. λ and cell capacity shown for cycle-aging at three characteristic frequencies: (A) 0.2 Hz, (B) 1 Hz and (C) 1 kHz.

$I_{AC2}=1.1$ C is shown over cycling at the characteristic frequencies. The progression of capacity fade over cycle-aging and the progression of λ measured at 1 Hz are in strong agreement. If the capacity decreases, λ decreases and if the capacity is constant, λ is constant, too. This characteristic correlation is not observed for the progression of capacity fade and the inverse of Y_{rms} , as already stated. Also, the progressions of λ measured at 0.2 Hz and 1 kHz, however, fluctuate and do not match the progression of capacity fade over cycle-aging. They even show strong fluctuations, rendering these frequencies as unsuitable for monitoring SOH.

As 1 Hz is in the frequency range of the electrochemical reactions, the correlation of λ to capacity may be correlated to the loss of the specific surface a_s of the electrode. If the capacity, respectively a_s , decreases and excitation amplitudes I_{AC} of the dynamic analysis are kept constant, the current flow per specific surface area, the volumetric current density, is higher. If the current density increases, cell overpotentials have to increase, as well. Consequently, increasing overpotentials cause an increase of Y_{rms} . This is observed for both excitation amplitudes I_{AC} that are used for dynamic analysis at the defined cycling steps ($I_{AC1}=50$ mA, $I_{AC2}=100$ mA). However, Y_{rms} does not increase linearly with higher I_{AC} . For smaller I_{AC} , the Y_{rms} increase is higher for decreasing capacity than for higher I_{AC} , which we will demonstrate in the following section using simulation. Consequently, λ will decrease for decreasing capacities.

Experiments vs. simulations.—As there is presently little knowledge about how to reliably interpret changes in NFR spectra, we here use physicochemical models to aid interpretation. This has already been successfully demonstrated by Wolff et al. and Murbach et al.^{20,24} for unaged spectra. Thus, in a next step, the correlation of λ and capacity fade is analyzed in-depth by using the reaction model, as introduced in reaction model section. A base case parameter set is given in Table I. As we focus on a model-based investigation of the reaction process, the double layer capacitance C_{DL} is chosen to get the best possible correlation of NFR measurements and simulations at the frequency characteristic for reaction, e.g. around 1 Hz in range Ib. Therefore, only the corresponding characteristic frequency range Ib between approximately 0.2 to 10 Hz is of interest in the following discussion. In a first step, amplitude dependency I_{AC} and its influence on NFRA are investigated prior to a simulative aging analysis via a variation of the specific surface area a_s .

In Figure 6A, simulated NFR spectra of a single reaction according to Butler-Volmer kinetics are shown for a variation of I_{AC} . Beginning with a frequency of approximately 10 Hz until 0.2 Hz, Y_{rms} increases in the simulations. This steep slope of Y_{rms} is observed in experiments in range Ib, as well. For frequencies smaller than 0.2 Hz and above 10 Hz, Y_{rms} is constant in the simulations due to the implementation of only one single electrochemical reaction with neglect of any transport processes, e.g. diffusion of Lithium-ions in the active

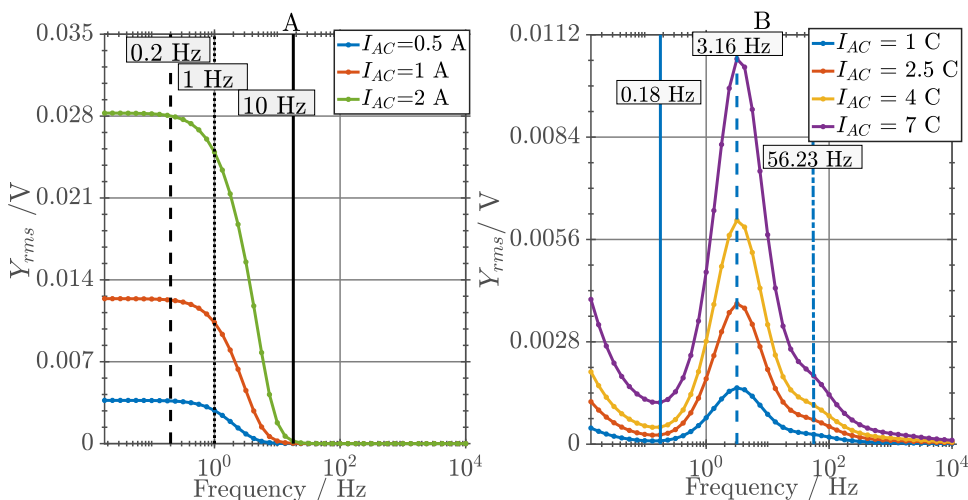


Figure 6. (A) NFRA simulations on the reaction model with current amplitudes 0.5 A, 1 A and 2 A and (B) NFRA simulations on a full model with current amplitudes of 1 C, (2), 5 C, 4 C and 7 C according to Wolff et al.²⁰

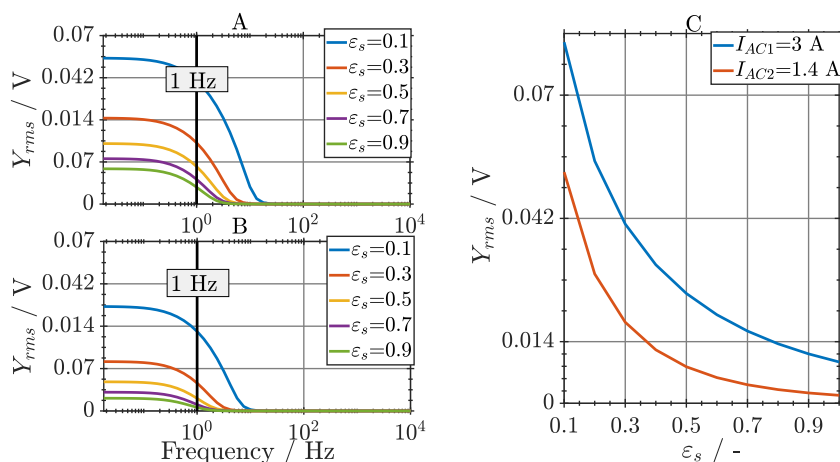


Figure 7. Impact of solid fraction on NFRA simulations for (A) $I_{AC1}=3$ A and for (B) $I_{AC2}=1.4$ as well as (C) at the specific frequency 1 Hz for a variation of ϵ_s .

material particles, as priorly discussed. In Table VI, characteristic frequency ranges of NFR simulations on the reaction model in comparison to NFR measurements are given. In contrast to this, our full model analysis, shown in Figure 6B, contains transport and showed similar steep increase of Y_{rms} in the low frequency range, shown in Figure 6B. The Figure 6B is taken from a study by Wolff et al., in which a standard Pseudo-2-dimension model with porous, structured electrodes has been used in a model-based analysis of the harmonic voltage responses of LIBs.³¹ Hereby, it is important to note that Wolff et al. analyzed NFR of the initial, transient part of the battery, which results in a peak-shaped progression of NFR in the frequency range characteristic for the electrochemical reaction, as surface concentration gradients and potentials at the interface between electrode and electrolyte are not in equilibrium yet.²⁰ In the presented study, however, the steady-state response of the battery is analyzed and therefore the electrochemical reaction process is already in equilibrium. Due to this, the characteristic progression differs. Still, the frequency range characteristic for the electrochemical reaction as well as the amplitudes of harmonic voltage responses are similar in the simulations with the reaction model and the P2D-model. The analysis of harmonic voltage responses of a LIB in a steady state with a full model, which also contains transport processes, is focus of ongoing work and out of scope in the work published by Wolff et al.²⁰ In general, however, analysis of NFRA simulations confirms the finding of the experimental process correlation. We thus expect to see changes in the specific surface area, and thus in kinetics, in range Ib. Any analysis of kinetic effects, and aging or design related changes in kinetics should therefore focus on this range.

In the reaction model, the variation of ϵ_s and therefore the variation of the specific surface area of the electrode a_s , according Equation 8, is used to analyze the impact of decreasing cell capacity on NFRA. The input excitation amplitude I_{AC} is kept constant for this variation. If ϵ_s and thus a_s decreases, Y_{rms} increases, as shown in Figures 7A and 7B for 3 A and 1.4 A. Thereby, it is shown that decreasing capacity due to loss of active material results in increased Y_{rms} , but does not affect the NFR spectrum in its characteristic progression. Further, in Figure 7C, Y_{rms} values at the characteristic frequency 1 Hz are shown for a broad variation of active material fraction ϵ_s and two excitation amplitudes I_{AC} . The simulations suggest that Y_{rms} extracted at specific frequencies increase exponentially with decreasing cell capacity. Y_{rms} increases over cycling in the experiments, as well. However, as discussed, experimental capacity has an unexpected non-monotonous behavior with cycling number whereas Y_{rms} increases monotonously. This feature cannot be reproduced with the modeled scenario of active area loss as cause for cycling based capacity fade. It remains open for now, which additional underlying aging-triggered changes in the cell cause the capacity increase. Further, a comparison of Y_{rms} in Figure 7C illustrates that for smaller I_{AC} , the relative Y_{rms} increase is higher for decreasing capacity, respectively ϵ_s , than for higher I_{AC} . For an excitation amplitude of $I_{AC}=1.4$ A, Y_{rms} increases

about 2 times for an decrease of $\epsilon_s=0.6$ to 0.4, but for an excitation amplitude of 3 A only approximately 1.6 times. This was observed in the experiments, as well. These simulations predict that λ decreases with decreasing ϵ_s , which is investigated in the following section.

Simulative aging analysis.—In the following, the correlation of λ and decreasing cell capacity is analyzed using the reaction model. NFRA simulations are conducted for a variation of excitation currents and active material fraction ϵ_s , and therefore for capacity loss according Equation 9. As in the experiments, the characteristic frequency of 1 Hz is chosen for the calculation of λ . As previously stated, we use a strongly simplified model, where only the kinetic of one single electrochemical reaction is implemented in the reaction model. A discharge capacity cannot be determined and thus, the adaption of the absolute excitation current in relation to a cell capacity is not possible, as it has been done in experimental studies. However, the relative excitation currents used in the reaction model have been set in correspondence to the experimental investigations. Further, to evaluate the sensitivity of λ to the excitation currents, multiple λ with different excitation amplitudes are simulated. The ratio of simulated and experimental λ (left y-axis) as well as capacities (right y-axis) are shown over cycle-aging in Figure 8. All simulated λ for decreasing ϵ_s show the same progression as the corresponding experimental λ for decreasing cell capacity. The simulated λ differ quantitatively due to the variation of the excitation amplitudes I_{AC} , but not qualitatively. The values for the NFR quotient λ gathered from the experimental study can be identified using AC excitations I_{AC} of 3 A and 1.4 A in the simulations. For these amplitudes, the quantitative differences between measured and simulated λ are approximately 5%, which is a good approximation regarding that a strongly simplified model was used for the simulations. In general, simulations with the reaction model confirm that changes in capacity due to loss of active material, respectively specific surface area can be correlated to λ , suggesting that this measure is in principle suitable to detect capacity losses with NFRA. λ measured at the characteristic frequency of 1 Hz, however, appears to be a reliable and accurate parameter for determining SOH decrease due to capacity loss.

Table VI. ω -range of NFR simulations on the reaction model in comparison to NFR measurements.

Range	ω_{sim} -range / Hz	ω_{exp} -range / Hz	Process
Ia	-	0.02 to 0.3	Solid diffusion
Ib	0.2 to 10	0.3 to 10	Electrochemical reactions
II	-	10 to 10k	Ionic transport processes between and in the SEI and electrolyte

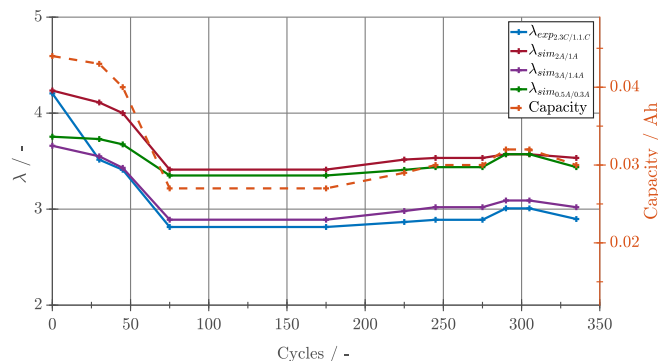


Figure 8. Measured and simulated λ at 1 Hz and cell capacity shown for cycle-aging.

In a last step, NFR spectra are simulated for a capacity loss by linearly decreasing ε_s and therefore the specific surface area a_s . Capacity loss is therefore presented via decreasing of the active material fraction ε_s . λ at the characteristic frequency 1 Hz is calculated accordingly as a function of ε_s . This allows to deduce a formula to calculate SOH from λ . In Figure 9A, it is shown that λ decreases almost linearly with decreasing ε_s , respectively the linear decreasing cell capacity, at the characteristic frequency of the electrochemical reaction. Thereby λ and the capacity decrease due to the reduction of the specific reaction surface of LIBs have an almost linear correlation. Therefore, λ at frequencies specific for the electrochemical reaction is identified as a good parameter for SOH estimation of LIBs, as given in Equation 10.

$$SOH = \frac{\lambda_x}{\lambda_{initial}} 100 \quad [10]$$

Conclusions

We present a novel approach for the estimation of capacity fade due to loss of specific surface area, e.g. due to loss of active material, and therefore the State of Health of a Lithium-ion Battery. A cycle-aging experiment was conducted at 25°C and the nonlinear dynamic measurement method, NFRA, was applied at two current amplitudes I_{AC} in defined cycle steps to study effects of aging on NFR spectra. The ratio of nonlinearities at those excitation amplitudes, λ , shows a very good qualitative correlation to the capacity fade over cycles in the characteristic frequency range of the electrochemical reaction. Therefore, a capacity decrease leads to a decreased relation of nonlinearities λ . If the capacity does not vary with cycle-aging, neither does λ . λ at 1 Hz was found to be an excellent parameter for this purpose. In contrast to this, the absolute Y_{rms} increases even if the cell

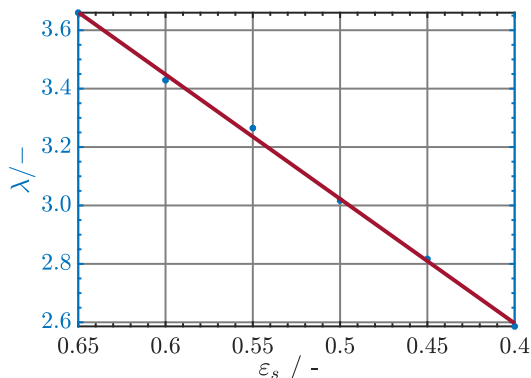


Figure 9. Simulated λ at 1 Hz for decreasing active material fraction ε_s , respectively a_s .

capacity stays constant for multiples cycles. Therefore, the overall nonlinearities of the cell seem not to be suitable for SOH estimation.

We further analyzed the finding from the experimental study in-depth by using NFRA on a reaction model with Butler-Volmer kinetics and with a dynamic charge balance at the electrode surface. NFRA simulations on the model support our experimental findings. Simulated λ for decreasing ε_s , which were adjusted in relation to the experimental measured cell capacities, showed a similar progression as λ from cycle-aging measurements.

Concluding, determining λ at one single frequency in the characteristic excitation range of the electrochemical reactions was found to be a suitable method for the estimation of capacity fade of LIBs. Therefore, using NFRA at two excitation amplitudes I_{AC} on battery systems may be a powerful diagnosis technique for the estimation of the SOH. Future studies are needed to evaluate the robustness of the method and whether the method is suitable for on-board diagnostic with a battery management system. If evaluated positive, NFRA may prove to be a low cost, fast and robust technique for estimating SOH.

Acknowledgments

The IGF project 8415 N/1 of the research association for Drive Technology (FVA e.V.) was funded by the German Federation of Industrial Research Associations (AiF) within the program Industrial Collective Research and Development (IGF) of the Federal Ministry of Economics and Technology (BMWi). Further, we thank for the support from the Battery LabFactory Braunschweig, especially the Institute for Particle Technology for manufacturing the electrodes and providing electrode parameters.

ORCID

Ulrike Krewer  <https://orcid.org/0000-0002-5984-5935>

References

1. C. Wu, C. Zhu, Y. Ge, and Y. Zhao. A Review on Fault Mechanism and Diagnosis Approach for Li-Ion Batteries. *Journal of Nanomaterials*, **2015**, (2015).
2. J. Vetter, P. Novak, M. R. Wagner, and C. Veit. Ageing Mechanisms in Lithium-Ion Batteries. *Journal of Power Sources*, **147**(1–2), 269 (2005).
3. V. Agubra and J. Fergus. Lithium ion battery anode aging mechanisms. *Materials*, **6**(4), 1310 (2013).
4. A. Barré, B. Deguilhem, S. Grolleau, M. Gérard, F. Suard, and D. Riu. A review on Lithium-Ion Battery Ageing Mechanisms and Estimations for Automotive Applications. *Journal of Power Sources*, **241**, 680 (2013).
5. C. Pastor-Fernández, K. Uddin, G. H. Chouchelamane, W. D. Widanage, and J. Marco. A Comparison between Electrochemical Impedance Spectroscopy and Incremental Capacity-Differential Voltage as Li-ion Diagnostic Techniques to Identify and Quantify the Effects of Degradation Modes within Battery Management Systems. *Journal of Power Sources*, **360**, 301 (2017).
6. S. M. Rezvanzaniani, Z. Liu, Y. Chen, and J. Lee. Review and recent advances in battery health monitoring and prognostics technologies for electric vehicle (EV) safety and mobility. *Journal of Power Sources*, **256**, 110 (2014).
7. Y. Zhou, M. Huang, Y. Chen, and Y. Tao. A novel health indicator for on-line lithium-ion batteries remaining useful life prediction. *Journal of Power Sources*, **321**, 1 (2016).
8. J. Remmlinger and M. Buchholz. State-of-Health Monitoring of Lithium-Ion Batteries in Electric Vehicles by on-board Internal Resistance Estimation. *Journal of Power Sources*, **196**(12), 5357 (2011).
9. J. Remmlinger, M. Buchholz, T. Soczka-Guth, and K. Dietmayer. On-board state-of-health monitoring of lithium-ion batteries using linear parameter-varying models. *Journal of Power Sources*, **239**, 689 (2013).
10. S. Sepasi, R. Ghorbani, and B. Y. Liaw. In-line state of health estimation of lithium-ion batteries using state of charge calculation. *Journal of Power Sources*, **299**, 246 (2015).
11. Y. Wang, R. Pan, D. Yang, X. Tang, and Z. Chen. Remaining Useful Life Prediction of Lithium-ion Battery Based on Discrete Wavelet Transform. *Energy Procedia*, **105**, 2053 (2017).
12. M. Dubarry, V. Svoboda, R. Hwu, and B. Yann Liaw. Incremental Capacity Analysis and Close-to-Equilibrium OCV Measurements to Quantify Capacity Fade in Commercial Rechargeable Lithium Batteries. *Electrochemical and Solid-State Letters*, **9**(10), A454 (2006).
13. T. Waldmann, A. Iturrondobeitia, M. Kasper, N. Ghanbari, F. Aguesse, E. Bekaert, L. Daniel, S. Genies, I. J. Gordon, M. W. Löhle, E. De Vito, and M. Wohlfahrt-Mehrens. Review—PostMortem Analysis of Aged Lithium-Ion Batteries: Disassembly Methodology and Physico-Chemical Analysis Techniques. *Journal of The Electrochemical Society*, **163**(10), A2149 (2016).

14. M. H. Hung, C. H. Lin, L. C. Lee, and C. M. Wang. State-of-Charge and State-of-Health Estimation for Lithium-Ion Batteries based on Dynamic Impedance Technique. *Journal of Power Sources*, **268**, 861 (2014).
15. T. Osaka, D. Mukoyama, and H. Nara. Review—Development of Diagnostic Process for Commercially Available Batteries, Especially Lithium Ion Battery, by Electrochemical Impedance Spectroscopy. *Journal of The Electrochemical Society*, **162**(14), A2529 (2015).
16. L. Lu, X. Han, J. Li, J. Hua, and M. Ouyang. A Review on the Key Issues for Lithium-Ion Battery Management in Electric Vehicles. *Journal of Power Sources*, **226**, 272 (2013).
17. D. Andre, M. Meiler, K. Steiner, Ch Wimmer, T. Soczka-Guth, and D. U. Sauer. Characterization of High-Power Lithium-ion Batteries by Electrochemical Impedance Spectroscopy. I. Experimental investigation. *Journal of Power Sources*, **196**(12), 5334 (2011).
18. A. M. Bond, N. W. Duffy, D. M. Elton, and B. D. Fleming. Characterization of Nonlinear Background Components in Voltammetry by use of Large Amplitude Periodic Perturbations and Fourier Transform Analysis. *Analytical Chemistry*, **81**(21), 8801 (2009).
19. N. Harting, N. Wolff, F. Röder, and U. Krewer. Nonlinear Frequency Response Analysis (NFRA) of Lithium-Ion Batteries. *Electrochimica Acta*, **248**(0), 133 (2017).
20. N. Wolff, N. Harting, M. Heinrich, F. Röder, and U. Krewer. Nonlinear Frequency Response Analysis on Lithium-Ion Batteries: Pseudo-Two-Dimensional Porous Electrode Model Based Investigation. **260**, 614 (2017).
21. Q. Mao and U. Krewer. Sensing Methanol Concentration in Direct Methanol Fuel Cell with Total Harmonic Distortion: Theory and Application. *Electrochimica Acta*, **68** (2012).
22. T. R. Vidakovic and V. V. Pani. Nonlinear Frequency Response Analysis of the Ferrocyanide Oxidation Kinetics. Part I. A *Theoretical Analysis*, **115**(35), 17341 (2011).
23. S. Okazaki. Second-Order Harmonic in the Current Response to Sinusoidal Perturbation Voltage for Lead-Acid Battery. *Journal of The Electrochemical Society*, **132**(7), 1516 (1985).
24. M. D. Murbach and D. T. Schwartz. Extending Newman's Pseudo-Two-Dimensional Lithium-Ion Battery Impedance Simulation Approach to Include the Nonlinear Harmonic Response. *Journal of The Electrochemical Society*, **164**(11), E3311 (2017).
25. M. D. Murbach, V. W. Wu, and D. T. Schwartz. Nonlinear Electrochemical Impedance Spectroscopy of Lithium-Ion Batteries: Experimental Approach, Analysis, and Initial Findings. *Journal of the Electrochemical Society*, **165**(11), A2758 (2018).
26. N. Harting, N. Wolff, and U. Krewer. Identification of lithium plating in lithium-ion batteries using Nonlinear Frequency Response Analysis (NFRA). *Electrochimica Acta*, **281**, 378 (2018).
27. N. Harting, R. Schenkendorf, N. Wolff, and U. Krewer. State-of-health identification of lithium-ion batteries based on nonlinear frequency response analysis: First steps with machine learning. *Applied Sciences*, **8**(5), 821 (2018).
28. Qing Mao, Ulrike Krewer, and Richard Hanke-Rauschenbach. Total Harmonic Distortion Analysis for Direct Methanol Fuel Cell Anode. *Electrochemistry Communications*, **12**(11), 1517 (2010).
29. V. V. Pani and T. R. Vidakovic. Nonlinear Frequency Response Analysis of the Ferrocyanide Oxidation Kinetics. Part II. *Measurement Routine and Experimental Validation*, **115**(35), 17352 (2011).
30. F. Röder, S. Sonntag, D. Schröder, and U. Krewer. Simulating the Impact of Particle Size Distribution on the Performance of Graphite Electrodes in Lithium-Ion Batteries. *Energy Technology*, **4**(12), 1588 (2016).
31. N. Legrand, S. Raël, B. Knosp, M. Hinaje, P. Desprez, and F. Lapique. Including Double-Layer Capacitance in Lithium-Ion Battery Mathematical Models. *Journal of Power Sources*, **251**, 370 (2014).
32. T. P. Heins, N. Harms, L. Schramm, and U. Schröder. Development of a new Electrochemical Impedance Spectroscopy Approach for Monitoring the Solid Electrolyte Interphase Formation. *Energy Technology*, **4**(12), 1509 (2016).
33. W. Mack Grady and S. Santoso. Understanding Power System Harmonics. *IEEE Power Engineering Review*, **21**(11), 8 (2001).
34. K. Uddin, L. Somerville, A. Barai, M. Lain, T. R. Ashwin, P. Jennings, and J. Marco. The impact of high frequency-high-current perturbations on film formation at the negative electrode electrolyte interface. *Electrochimica Acta*, **233**, 1 (2017).
35. K. Uddin, A. D. Moore, A. Barai, and J. Marco. The effects of high frequency current ripple on electric vehicle battery performance. *Applied Energy*, **178**, 142 (2016).
36. D. P. Abraham, J. L. Knuth, D. W. Dees, I. Bloom, and J. P. Christophersen. Performance Degradation of High-Power Lithium-Ion Cells—Electrochemistry of Harvested Electrodes. *Journal of Power Sources*, **170**(2), 465 (2007).
37. F. Yang, D. Wang, Z. Yang, K. Tsui, and S. J. Bae. A study of the relationship between coulombic efficiency and capacity degradation of commercial lithium-ion batteries. *Energy*, **145**, 486 (2018).